

Article

Study on the Stress Distribution Characteristics of Rock in the Bottomhole and the Influence Laws of Various Parameters Under the Impact of a Liquid Nitrogen Jet

Bo Xiao ¹, Chengzheng Cai ^{2,3,*} , Yanan Gao ^{2,4,*}, Bo Wang ³, Yinrong Feng ³, Jiacheng Li ³ and Zengxin Zou ⁵

¹ Sinopec Key Laboratory of Drilling Completion and Fracturing of Shale Oil and Gas, Sinopec Research Institute of Petroleum Engineering Co., Ltd., Beijing 102206, China

² YunLong Lake Laboratory of Deep Underground Science and Engineering, Xuzhou 221006, China

³ State Key Laboratory of Intelligent Construction and Healthy Operation & Maintenance of Deep Underground Engineering, China University of Mining and Technology, Xuzhou 221116, China

⁴ Carbon Neutrality Institute, China University of Mining and Technology, Xuzhou 221116, China

⁵ School of Low-Carbon Energy and Power Engineering, China University of Mining and Technology, Xuzhou 221116, China

* Correspondence: caicz@cumt.edu.cn (C.C.); yngao@cumt.edu.cn (Y.G.)

Abstract: This study presents research on the stress distribution characteristics of rock in the bottomhole and the influence laws of various parameters under the impact of liquid nitrogen jet. A multi-field coupled numerical model considering transient flow field, conjugate heat transfer, and nonlinear solid deformation was established to investigate the damage-induced fracturing mechanism of rock under liquid nitrogen jet. The study compares the impact effects of liquid nitrogen jet and water jet on rock and analyzes the variations in the stress field under different parameters. Due to its extremely low temperature, the liquid nitrogen jet creates a strong thermal stress gradient in a short time, significantly increasing the maximum principal stress and Mises stress in the rock compared to a water jet. Solid parameters, particularly the confining pressure and elastic modulus of the rock, have a more significant impact on stress distribution, while fluid parameters such as outlet pressure and fluid temperature have a smaller and more volatile effect. An increase in confining pressure inhibits tensile failure in the rock, while a higher elastic modulus enhances both tensile and shear failure. The initial rock temperature significantly affects the stress distribution, with optimal tensile failure observed at intermediate temperatures. The liquid nitrogen jet achieves a higher maximum velocity and overflow velocity than the water jet, contributing to more effective rock fracturing. The results provide a theoretical basis for the optimization of liquid nitrogen jet drilling parameters, which can help improve drilling efficiency.

Keywords: liquid nitrogen jet; flow field; stress distribution; parameter analysis



Citation: Xiao, B.; Cai, C.; Gao, Y.; Wang, B.; Feng, Y.; Li, J.; Zou, Z. Study on the Stress Distribution Characteristics of Rock in the Bottomhole and the Influence Laws of Various Parameters Under the Impact of a Liquid Nitrogen Jet. *Processes* **2024**, *12*, 2326. <https://doi.org/10.3390/pr12112326>

Academic Editor: Qingbang Meng

Received: 18 September 2024

Revised: 11 October 2024

Accepted: 21 October 2024

Published: 23 October 2024



Copyright: © 2024 by the authors. Licensee MDPI, Basel, Switzerland. This article is an open access article distributed under the terms and conditions of the Creative Commons Attribution (CC BY) license (<https://creativecommons.org/licenses/by/4.0/>).

1. Introduction

Since the Industrial Revolution, the extensive use of fossil fuels and the resulting greenhouse gas emissions have exacerbated global warming. In response, China has committed to reaching the peak of CO₂ emissions by 2030 and achieving carbon neutrality by 2060 [1]. Geothermal energy, as a clean energy source, is abundant in China but has low exploitation efficiency [2]. Exploiting the geothermal resource of hot, dry rock is a crucial objective for optimizing the energy structure, conserving energy, and reducing emissions; however, it presents significant challenges. Hydraulic fracturing is the primary technique used, but it faces several issues [3]. Hydraulic fracturing technology requires the consumption of vast amounts of freshwater resources, which are often difficult to recycle and reuse, resulting in the wastage of water resources. A single well typically consumes millions of liters of water, equivalent to the daily water usage of thousands of people.

The fracturing fluids used in the hydraulic fracturing process contain a large number of chemical additives, and these chemicals have the potential to contaminate soil and groundwater resources. Once wastewater leaks, it can pollute drinking water sources, posing a threat to the ecological environment and residents' health. Additionally, the cost of treating wastewater generated by hydraulic fracturing is high. Due to the high concentration of chemicals in this wastewater, treatment is extremely difficult and might even be beyond the capabilities of large-scale wastewater treatment plants. Therefore, researchers have proposed waterless fracturing methods [4–9], with liquid nitrogen fracturing standing out due to its ability to generate thermal stress, which promotes crack propagation in reservoirs at extremely low temperatures. Liquid nitrogen is readily available and cost-effective, making the liquid nitrogen fracturing technique promising. For deep reservoirs, liquid nitrogen jet-assisted fracturing has been proposed to reduce fracture initiation pressure and enhance rock-breaking efficiency [10]. Hot dry rock refers to deep underground rocks characterized by high temperatures, strong abrasiveness, and low permeability. Therefore, efficiently extracting heat from hot dry rock reservoirs requires efficient drilling and completion engineering. Currently, hydraulic-assisted drilling is the most used technique for reservoir breaking and well building. The working principle involves injecting water as the drilling fluid into the target reservoir to alter its stress field by increasing water pressure and expanding the breaking area [11].

With increasing concern for environmental protection and water resource conservation, waterless drilling and fracturing methods have begun to attract attention. Among these, liquid nitrogen jetting, as a novel and efficient method for rock breaking and hole formation, shows promising application prospects in assisting drilling acceleration and jet fracturing. Liquid nitrogen demonstrates significant advantages in enhancing rock cracking and breaking compared to traditional methods. For example, it has been applied in unconventional reservoir fracturing in the United States [12,13]. McDaniel et al. [12] indicated that when liquid nitrogen contacts high-temperature reservoirs, it creates a strong cold impact, causing the generation and propagation of fractures on the rock surface. This indicated that the injection of low-temperature liquid nitrogen into the well bottom through pipelines is feasible and operationally viable. Finnie et al. [14] focused on the influence of transient cooling on fracture initiation and expansion and found that cracks are more likely to form at pore edges under thermal impact. Thereby, it was confirmed that the use of rapid cooling methods could accelerate the fracturing of rocks. Ren et al. [15] observed a significant increase in permeability, along with changes in the internal strength and structural characteristics of coal rock, by cold impacting the coal rock with liquid nitrogen. Kim et al. [16] further demonstrated that rapid cooling of a hot rock alters thermal distribution, with significant tensile stresses appearing on the outer surface of the sample, contributing to the formation of microcracks. This indicated that the liquid nitrogen cooling method was able to weaken the mechanical strength of the rock and alter its crack distribution state. Cai et al. [17] employed nuclear magnetic resonance to analyze changes in the mechanical parameters of sandstone, shale, and coal rock after liquid nitrogen cooling. They revealed that liquid nitrogen not only induced cracks on the surface of the rock samples but also facilitated the propagation of pre-existing cracks, with permeability enhancement positively correlated with water content. This indicated that under the effect of rapid cooling with liquid nitrogen, significant changes occurred in the pore structure within the rock. Cha et al. [18] confirmed the feasibility of low-temperature fracturing in the reservoir by developing a liquid nitrogen fracturing test device. In addition, they observed that the pore structure within the rock is influenced by the temperature gradient created by liquid nitrogen, and the main fracture direction in low-temperature fracturing does not necessarily align with the principal stress direction. It can be seen that when liquid nitrogen is used for stratum rock breaking and drilling, the low-temperature cracking effect produced by liquid nitrogen helps to improve the efficiency of rock fragmentation. However, the analysis of the rock fracture mechanism was mainly conducted from the perspective of temperature changes, without addressing the aspect of stress distribution. In addition, the

aforementioned experimental studies primarily focused on the cooling effect of stationary liquid nitrogen and were not able to accurately reflect the cooling and cracking effect of high-speed flowing liquid nitrogen.

The liquid nitrogen jet, which combined the dual mechanisms of high-speed impact and low-temperature fracturing, exhibited significantly different rock-breaking characteristics from traditional water jets. Cai et al. [19,20] explored the impact of a liquid nitrogen jet on reservoir fracturing through numerical simulation and compared it to a water jet. The results indicated that abrasive particles in the liquid nitrogen jet achieved better acceleration and that the rock experienced more severe damage due to thermal stress under the low temperature of liquid nitrogen. The feasibility of forming a liquid nitrogen jet under downhole conditions was demonstrated by this research. Zhang et al. [21] established a coupled model to study the effects of liquid nitrogen cooling on coal bodies and discovered that low temperatures significantly increased the permeability of coal rock, with damage and deformation intensifying closer to the borehole. Huang et al. [22] investigated the effect of nozzle parameters on particle velocity in liquid nitrogen abrasive jets, while Li et al. [23] proposed utilizing liquid nitrogen vaporization to fracture shale reservoirs as a solution to water resource limitations and environmental concerns. The feasibility of forming a liquid nitrogen jet under downhole conditions was demonstrated by this research. Zhai et al. [24,25] experimentally verified that the time and cycle of liquid nitrogen freezing increase with higher effective and total porosity of coal. Yao et al. [26] employed TOUGH2-EGS to simulate liquid nitrogen fracturing for enhanced production and found that the high-pressure injection of low-temperature fluid significantly improves reservoir permeability. Cai et al. [27,28] analyzed the flow field characteristics of liquid nitrogen jets through laboratory experiments and demonstrated their superior impact performance compared to water jets. Experiments by Wu [29] on coal fracturing with a liquid nitrogen jet also showed that the volume of crushed coal under the impact of a liquid nitrogen jet was greater than that under the impact of the water jet. The experimental results indicated that the combined effects of low-temperature fracturing and the high-speed impact of the liquid nitrogen jet effectively enhanced the efficiency of rock fragmentation. Numerical simulations by Zhang et al. [30,31] revealed that the thermal stress generated by temperature gradients reduced rock fracture pressure and promoted crack formation. They further simulated hot dry rock reservoirs with a liquid nitrogen abrasive jet and conducted experiments. They concluded that the combined effects of low temperature, high pressure, and abrasives in the liquid nitrogen abrasive jet caused severe damage to high-temperature rock, forming intricate pore networks [32,33]. The research findings revealed the effect of thermal stress on rock fracturing during the impact of liquid nitrogen jets, further elucidating the differences in rock-breaking mechanisms between liquid nitrogen jets and water jets. Yang et al. [34] conducted a series of gas fracturing tests on granite samples treated with a liquid nitrogen abrasive jet. They demonstrated that the rock samples treated with the liquid nitrogen abrasive jet experienced significant changes in fracture pressure. After the coal body was treated with the liquid nitrogen abrasive jet, staggered fracture networks gradually formed on the coal surface, improving reservoir permeability. Liu et al. [35] proposed a novel water–liquid nitrogen (W-LN₂) jet method and revealed concrete’s crushing rules and crack characteristics at macro and micro levels. Their results indicated that a W-LN₂ jet increases crushing pit width by 139.25%, depth by 21.65%, and volume by 59.68% compared to a pure water jet (PWJ). Wang et al. [36] designed an experimental platform to study the surface heat transfer induced by the liquid nitrogen jet and calculated the temperature-dependent surface heat transfer coefficient (T-SHTC) using an inverse heat conduction theory. They found that factors like LN₂ mass flow, jet distance, and nitrogen phase influence SHTC, with jet distance being more significant. Dai et al. [37] conducted experiments to study rock failure under cutting and jet impingement. The results showed that jet impact, especially LN₂ with its cryogenic properties and low viscosity, induced thermal stress and improved rock-breaking efficiency more than the water jet. The cutting force reduced by 43.96% with the water jet and by 52.53% with the LN₂ jet. Cai et al. [38] investigated the impact of a

liquid nitrogen jet (LNJ) and liquid nitrogen immersion (LNI) cooling on high-temperature granite. The results showed that mechanical properties deteriorated more with increasing temperature and cooling cycles for both methods. However, LNI's effect weakened with cycles, while LNJ's deteriorated significantly. This indicated that there were significant differences in the fracturing mechanisms between liquid nitrogen jet cooling and immersion cooling. Li et al. [39] experimentally investigated the transient cooling of rock surfaces using liquid nitrogen (LN_2) jets. The results showed sharp thermal gradients and tensile thermal stresses, with a maximum tensile stress of 5 MPa, potentially damaging the rock structure and reducing its strength. The aforementioned research findings primarily focused on the flow field characteristics and differences in rock-breaking effects between liquid nitrogen jets and water jets, with limited exploration of the underlying mechanical mechanisms involved.

In summary, current research on liquid nitrogen jets has primarily concentrated on aspects such as jet flow field characteristics and rock fragmentation features. However, the differences in flow field characteristics between liquid nitrogen jets and water jets result in distinct stress distributions on the rock surface, thereby influencing the stress state of the rock at the wellbore bottom and leading to variations in rock-breaking effects. Therefore, to better elucidate the rock-breaking mechanism of liquid nitrogen jets and subsequently identify the key factors affecting the impact effectiveness of liquid nitrogen jets, it is necessary to analyze the impact characteristics and key influencing factors of liquid nitrogen jets from the perspective of stress distribution. This analysis should not merely focus on the impact pressure of the jet on the rock surface but should shift its emphasis to the stress distribution on and within the rock surface. This study aims to utilize the finite element method to construct numerical models of impacting flow fields in the bottomhole under liquid nitrogen and water jets and to compare the distribution characteristics of impact velocity, pressure, temperature, and overflow velocities under both jets. In addition, the stress fields of rock under the impact of both jets are simulated and analyzed to explore the differences in their effects on the rock stress field in the bottomhole, providing theoretical support for understanding the differences between liquid nitrogen and water jets in rock-fracturing effects. In addition, this study investigates the influence of various parameters on the maximum principal stress and Mises stress of rock, aiming to offer a scientific basis for the optimized design of liquid nitrogen jet parameters.

2. Numerical Model

2.1. Problem Description and Geometric Model

The high-pressure jet drilling technique, which utilizes jet impact to fracture rock, offers multiple advantages, including a low cost, high efficiency, and environmental friendliness. This technique primarily employs high-pressure water jets to achieve the desired impact. However, due to their low-temperature properties, research reveals that liquid nitrogen jets can induce thermal stress in the rock, enhancing fracturing efficiency. Therefore, this study develops a model using water and liquid nitrogen as impact fluids to investigate their effects. Given that the impact of a liquid nitrogen jet on rock is a complex multi-field coupling process involving transient flow fields, conjugate heat transfer, and solid nonlinear deformation, this study focuses on the coupling of thermal stress and jet impact pressure to reveal the underlying mechanisms of rock fracturing by liquid nitrogen jets.

A geometric model is established to thoroughly analyze the fluid velocity, pressure, and temperature fields of high-temperature rock during the impact of water and liquid nitrogen jets in the bottomhole, as shown in Figure 1. The model consists of the solid and fluid domains, where the fluid domain encompasses the region inside the nozzle and the impact area of the wellbore annulus. The space between the nozzle outlet and the bottomhole is the underground region, while the space between the drill rod and rock mass is considered the annular region. The solid domain primarily represents the rock surrounding the wellbore, including the surrounding rocks and rock masses in the bottomhole. The nozzle design features a symmetrical structure composed of conical and

cylindrical sections. The distance from the nozzle outlet to the bottomhole is the jet distance. Based on gas drilling technology, during jet drilling operations, the high-pressure jet enters the nozzle and underground region through the nozzle inlet and accelerates to form a high-speed jet at the outlet. This high-speed jet significantly impacts the rock in the bottomhole and then flows out through the annular region. This study defines the jet centerline and its extension line as axial, while the direction perpendicular to the jet centerline is referred to as radial. The specific parameters of the model are listed in Table 1.

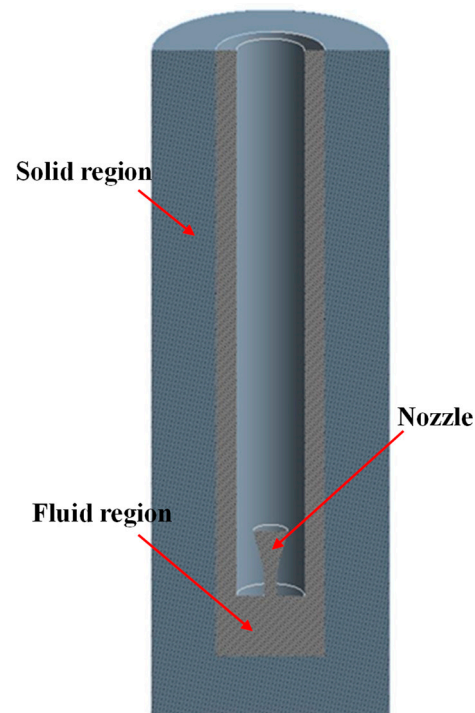


Figure 1. The model for the flow and stress fields in the bottomhole.

Table 1. Parameters of the model.

Wellhole Height	Borehole Diameter	Drill Pipe Diameter	Rock Mass Thickness	Total Model Height	Nozzle Jet Distance	Nozzle Outlet Diameter
300 mm	50.8 mm	31.8 mm	30 mm	330 mm	30 mm	6 mm

2.2. Mathematical Model

Both liquid nitrogen and water jets impacting high-temperature rock in the bottomhole involve fluid flow and convective heat transfer. The mathematical model is related to fluid viscosity, flow velocity, density, thermal conductivity, specific heat capacity, and other factors.

(1) Fluid region

The liquid nitrogen jet process involves heat transfer and fluid compressibility. Therefore, the energy equation must also be solved in addition to the mass conservation and momentum equations. During the impact of the liquid nitrogen jet, the pressure and temperature in the flow field undergo rapid changes. These sudden changes in pressure and temperature affect the physical properties of liquid nitrogen and nitrogen gas, influencing the characteristics of the flow field. A more precise model for calculating the physical properties of liquid nitrogen and nitrogen gas is employed during the calculations to enhance computational accuracy.

Given the high Reynolds number of liquid nitrogen jets, the turbulence model provides high accuracy and stability for fully developed turbulent flow at high Reynolds numbers.

$$\frac{\partial(\rho k)}{\partial t} + \text{div}(\rho U k) = \text{div} \left[\left(\mu + \frac{\mu_t}{\sigma_k} \right) \cdot \text{grad} k \right] - \rho \varepsilon + \mu_t P_G \quad (1)$$

$$\frac{\partial(\rho \varepsilon)}{\partial t} + \text{div}(\rho U \varepsilon) = \text{div} \left[\left(\mu + \frac{\mu_t}{\sigma_\varepsilon} \right) \cdot \text{grad} \varepsilon \right] - \rho C_2 \frac{\varepsilon^2}{k} + \mu_t C_1 \frac{\varepsilon}{k} P_G \quad (2)$$

where k and ε are the turbulent kinetic energy and dissipation rate, respectively; σ_k , σ_ε , C_1 , and C_2 , are constants, and their values are generally taken as $\sigma_k = 1.0$, $\sigma_\varepsilon = 1.3$, $C_1 = 1.44$, and $C_2 = 1.92$ in numerical calculations; and μ_t is the turbulent viscosity. μ_t and P_G can be expressed as follows:

$$\mu_t = \rho C_\mu \frac{k^2}{\varepsilon}, P_G = 2S_{ij} \cdot S_{ij} \quad (3)$$

The continuity equation can be expressed as

$$\frac{\partial \rho_f}{\partial t} + \frac{\partial(\rho_f u_i)}{\partial x_i} = 0 \quad (4)$$

The momentum conservation equation can be expressed as

$$\frac{\partial(\rho_f u_i)}{\partial t} + \frac{\partial(\rho_f u_i u_j)}{\partial x_j} = -\frac{\partial p}{\partial x_i} + \frac{\partial}{\partial x_i} \left(\mu \frac{\partial u_i}{\partial x_i} \right) + S_i \quad (5)$$

The energy conservation equation can be expressed as

$$\frac{\partial(\rho_f T_f)}{\partial t} + \frac{\partial(\rho_f u_i)}{\partial x_i} = S_T + \frac{\partial}{\partial x_i} \left(\frac{k_h}{c_p} \frac{\partial T_f}{\partial x_i} \right) \quad (6)$$

where t is the time; ρ is the density; u is the velocity component; x is the displacement component; μ is the hydrodynamic viscosity of fluid; k_h is the fluid thermal conductivity; c_p is the fluid specific heat; and s_i and s_T are the source terms of the momentum and energy conservation equations, respectively.

Heat exchange occurs between the fluid and the rock, and conjugate heat transfer is employed to calculate heat transfer at the fluid–solid interface. Since the heat fluxes at the interface are identical, the governing equation for fluid thermal conductivity can be derived as follows:

$$\begin{cases} q_w|_{solid} = q_w|_{fluid} \\ -k_s \left(\frac{\partial T_s}{\partial n} \right)_w|_{solid} = k_h (T_w - T_{adj})|_{fluid} \end{cases} \quad (7)$$

where q_w is the heat flux at the flow–solid surface; k_s is the heat transfer coefficient of the fluid at the wall surface; and T_w and T_{adj} are the rock temperature at the flow–solid coupling surface and the near-wall fluid temperature, respectively.

(2) Solid region

As heat transfer occurs in the rock in the solid region, solving the heat transfer equation for the solid region is necessary.

$$k_s \nabla^2 T_s = c_s \rho_s \frac{\partial T_s}{\partial t} \quad (8)$$

where k_s is the heat transfer coefficient of the wall surface to the fluid; T_s is the temperature of the rock; ρ_s is the density of the rock; and c_s is the specific heat capacity of the rock.

The impact pressure from the jet affects the stress field within the rock. In addition, due to heat transfer in the solid region, varying temperatures influence the thermal stress state within the rock. It is necessary to solve the physical, equilibrium, and compatibility equations for thermal stress calculations in the solid region. The governing equations are as follows:

Physical equation:

$$\varepsilon_{ij} = \frac{1}{2G} \left(\sigma_{ij} - \frac{\nu}{1+\nu} \sigma_{kk} \delta_{ij} \right) + \alpha \Delta T_s \delta_{ij} \quad (9)$$

Equilibrium equation:

$$\left(\frac{E\nu}{(1+\nu)(1-2\nu)} + G \right) \nabla^2 e - \frac{\alpha E}{1-2\nu} \nabla^2 T_s = 0 \quad (10)$$

Compatibility equation:

$$\begin{cases} \nabla^2 \sigma_i + \frac{1}{1+\nu} \frac{\partial^2 \sigma_{ii}}{\partial x_i^2} = 1\alpha E \left(\frac{1}{1-\nu} \nabla^2 T_s + \frac{1}{1+\nu} \frac{\partial^2 T_s}{\partial x_i^2} \right) \\ \nabla^2 \tau_{ij} + \frac{1}{1+\nu} \frac{\partial^2 \sigma_{ii}}{\partial x_i \partial x_{ij}} = \left(\frac{\alpha E}{1+\nu} \frac{\partial^2 T_s}{\partial x_i \partial x_j} \right) \end{cases} \quad (11)$$

where k_s is the heat transfer coefficient of the wall surface to the fluid; T_s is the temperature of the rock; ρ_s is the density of the rock; c_s is the specific heat capacity of the rock; E is the modulus of elasticity; G is the shear modulus; ν is the Poisson's ratio of the rock; α is the thermal expansion coefficient; ε_{ij} is the strain in the rock; σ_{ij} is the rock stress; ν is the Poisson's ratio of the rock; σ_{kk} is the sum of the total stresses; δ_{ij} is the Kroenke's symbol (its value is specified as 1 for $i = j$ and 0 for $i \neq j$); α is the thermal expansion coefficient; ΔT_s is the temperature difference in the rock; F_i is the volumetric force in the i -direction; and u_i is the displacement in the i -direction.

2.3. Mesh Division and Boundary Conditions

Figure 2 indicates that the geometric model in Figure 1 is meshed using triangular elements. The mesh is refined at this interface to enhance computational convergence and accuracy to facilitate the convergence of results at the fluid–solid coupling interface.

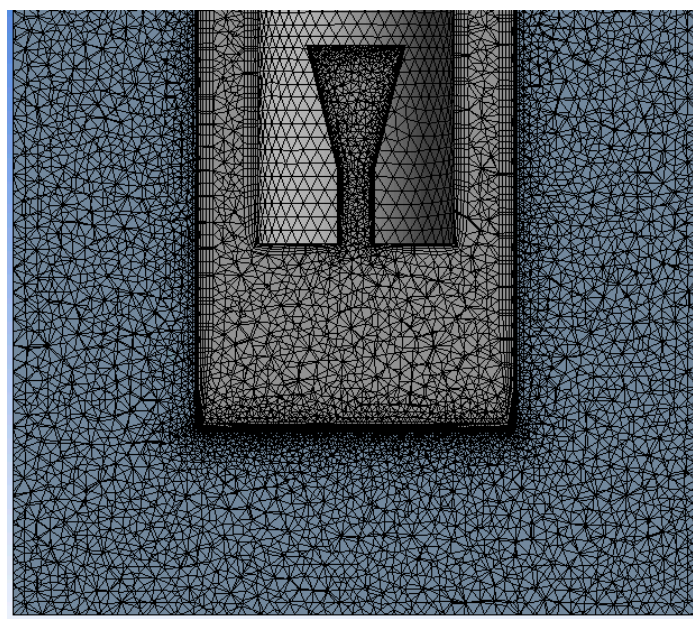


Figure 2. Mesh division.

The nozzle inlet in the simulation is designated as the pressure inlet boundary, while the wellhole annular outlet is set as the pressure outlet boundary. The interface between the fluid and solid regions is defined as the fluid–solid conjugate boundary, ensuring that the temperatures and heat fluxes of the fluid and solid remain consistent at this boundary while the remaining areas are set as wall boundaries. During the impact of the liquid nitrogen jet, a significant temperature difference between the liquid nitrogen and the deep hot rock results in a strong cold impact effect on the rock, causing energy exchange. Therefore, activating the energy equation and considering heat transfer boundary conditions is necessary under this condition. In addition, under high-speed jet conditions, the low-temperature liquid nitrogen entering from the nozzle generates turbulence in the flow field at the bottomhole; thus, the k - ε model is used for turbulence calculations. Since the deformation of the solid region is not considered, the boundary at the bottomhole in the solid domain is set as a fixed constraint to limit its degrees of freedom. The fluid–solid contact surface is the coupling surface, consistent with the fluid region, while the side boundaries are adiabatic, with zero heat flux.

2.4. Model Parameter Settings and Calculation Process

The inlet temperature, inlet pressure, outlet pressure, initial fluid temperature, initial rock temperature, fluid density, fluid viscosity, thermal conductivity, and specific heat capacity for both fluids (water and liquid nitrogen) are defined. The baseline calculation conditions are detailed in Table 2.

Table 2. Parameters for the fluid region.

Parameter Settings	Liquid Nitrogen Jet	Water Jet
Inlet pressure (MPa)	45	45
Outlet pressure (MPa)	25	25
Initial fluid temperature (K)	110	298.15
Initial rock temperature (°C)	150	150
Density (kg/m ³)	806.08	998.2
Viscosity (Pa·s)	1.6065×10^{-4}	10.03×10^{-4}
Thermal conductivity (W/m·K)	0.14581	0.6
Specific heat capacity (kJ/kJ·K)	2.0415	4.182

The density, specific heat capacity, heat conductivity coefficient, elastic modulus, and Poisson's ratio for the solid region are defined as listed in Table 3.

Table 3. Parameters for the solid region.

Density	Specific Heat Capacity	Heat Conductivity Coefficient	Elastic Modulus	Poisson's Ratio
2300 kg/m ³	760 J/(kg·K)	2.5 W/(m·K)	30 Gpa	0.25

3. Characteristics of the Impact Flow Field in the Bottomhole

The flow and heat transfer characteristics in the bottomhole were analyzed under baseline conditions, with an inlet pressure of 45 MPa and an outlet pressure of 25 MPa. Since the flow field structure stabilizes after 10 s, choosing any time after 10 s is sufficient; the simulation time in this section is set to 10 s. The significant temperature difference between the water jet and the liquid nitrogen jet results in noticeable variations in physical parameters during heat transfer with the surrounding rock.

3.1. Velocity Field

A curve depicting velocity variation along the axis was derived to compare the velocity changes along the axial direction of water and liquid nitrogen jets, as depicted in Figure 3. At the right end of the figure, specifically at the nozzle inlet, the velocities of both jets are nearly identical. As the nozzle diameter gradually narrows, the jet velocities increase, forming an acceleration segment and reaching their peak at the nozzle outlet. Then, the jets are expelled at a constant

maximum velocity over a distance, creating a constant velocity segment. As the jets approach the bottomhole, their velocity declines rapidly, forming an impact segment. The lengths of these three segments for the water and liquid nitrogen jets are nearly the same. However, in the constant velocity segment, the velocity of the water jet is approximately 20 m/s slower than that of the liquid nitrogen jet. This difference can be attributed to the fact that, under identical jet pressure differences and nozzle sizes, the dynamic viscosity of liquid nitrogen is lower than that of water, resulting in relatively less kinetic energy dissipation due to viscous forces during the jetting process of the liquid nitrogen jet.

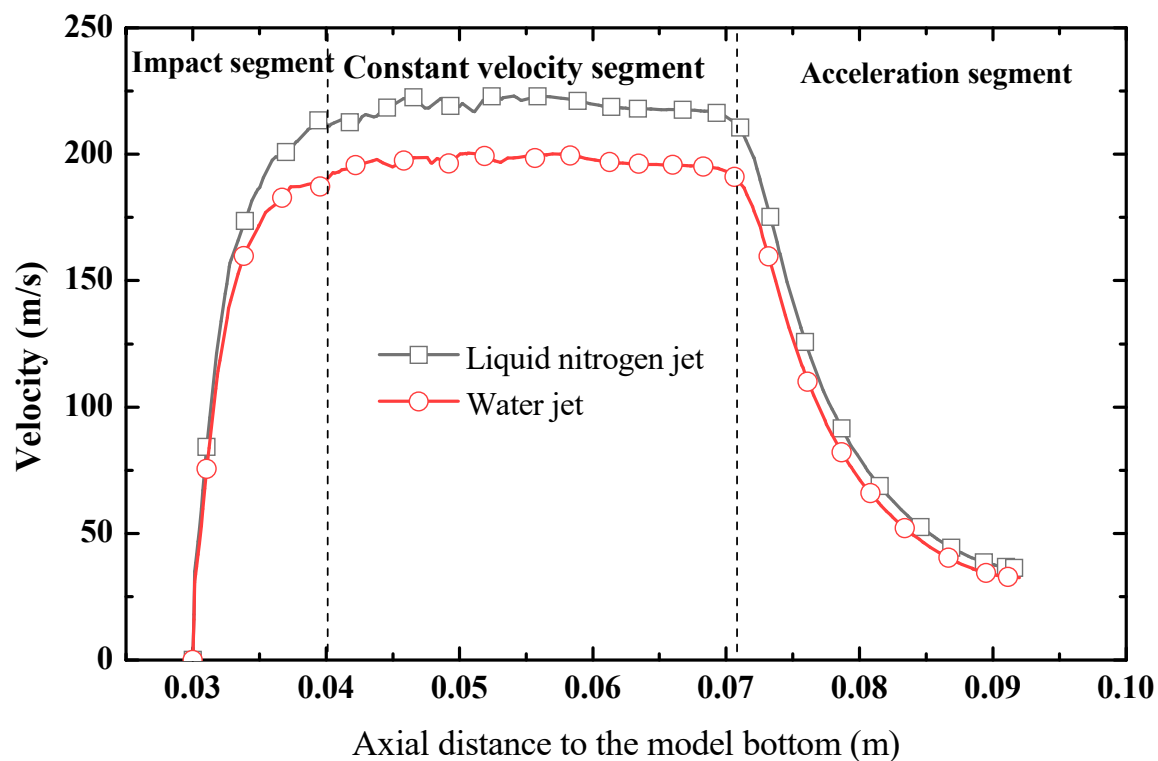


Figure 3. Curves of velocities along the axis.

3.2. Pressure Field

Figure 4 indicates that the pressure distributions created in the bottomhole by the water jet and liquid nitrogen jet exhibit similar characteristics. The pressure in the central region of the bottomhole is the highest, reaching 43 MPa, primarily due to the direct impact of the high-speed jets on the bottomhole. Then, the pressure gradually decreases in the radial direction, reaching a minimum of 23.5 MPa. However, the pressure near the edges, close to the surrounding rock, rises again to about 37.5 MPa, which results from the tangential velocity of the jets impacting the surrounding rock. The fluid pressure distribution in different regions of the bottomhole is uneven, leading to a varied pressure impact on the rock in the bottomhole. Specifically, the pressure at the center of the bottomhole is nearly twice that at its edge. This distribution pattern, where the center undergoes high compression while the edges experience lower pressure, significantly compresses the rock at the bottomhole center and facilitates its fracturing. The pressure distribution characteristics generated by the water jet and liquid nitrogen jet in the bottomhole play a significant role in rock fracturing, aiding in rock breakage and providing favorable conditions for subsequent drilling operations.

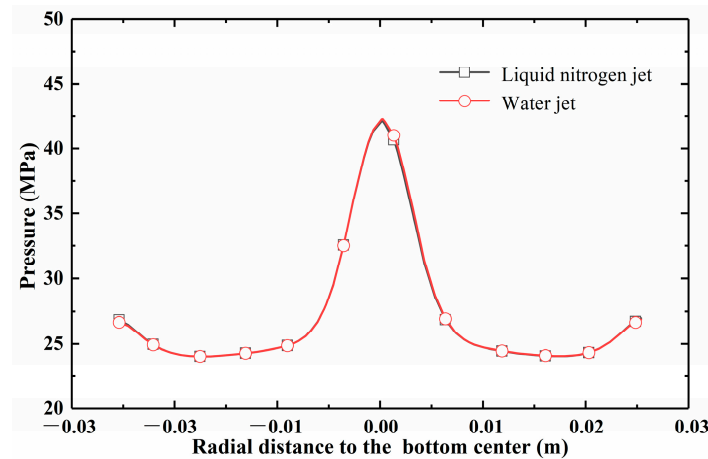


Figure 4. Curve of pressures in the bottomhole.

3.3. Overflow Velocity Field

After impacting the bottomhole, the jets generate a high-velocity overflow along the bottomhole, exerting significant shear effects on the rock within the bottomhole and enhancing the convective heat transfer between the jets and the rock. Considering the tangential velocity approximately 3 mm above the bottomhole as the subject of analysis, this study compares the tangential velocity characteristics in the bottomhole for both jets, and the velocity variations along the diameter of the bottomhole are depicted in Figure 5. The analysis reveals that the tangential velocity of both jets shows a symmetrical distribution, characterized by an acceleration segment where it rapidly rises from 0 m/s, a fluctuation segment with a peak velocity, and a deceleration segment where it quickly drops to 0 m/s near the surrounding rock at both ends. At the same location, the tangential velocity of the liquid nitrogen jet is significantly higher than that of the water jet. For instance, at a distance of 15 mm from the bottomhole center, the tangential velocity of the liquid nitrogen jet surpasses that of the water jet by approximately 6 m/s, marking an increase of nearly 20%, which indicates a more pronounced trend of velocity increase. The shear effect of the jet within the bottomhole directly affects its heat transfer with the rock. Variations in tangential velocity across the acceleration, fluctuation, and deceleration segments lead to significant differences in convective heat transfer along these paths, resulting in uneven thermal stress distribution and exacerbating the rock fracturing effect. Specifically, the lower tangential velocity of the water jet compared to the liquid nitrogen jet results in a higher convective heat transfer rate for the liquid nitrogen jet, leading to a more significant impact on thermal stress in the rock and a more pronounced fracturing effect.

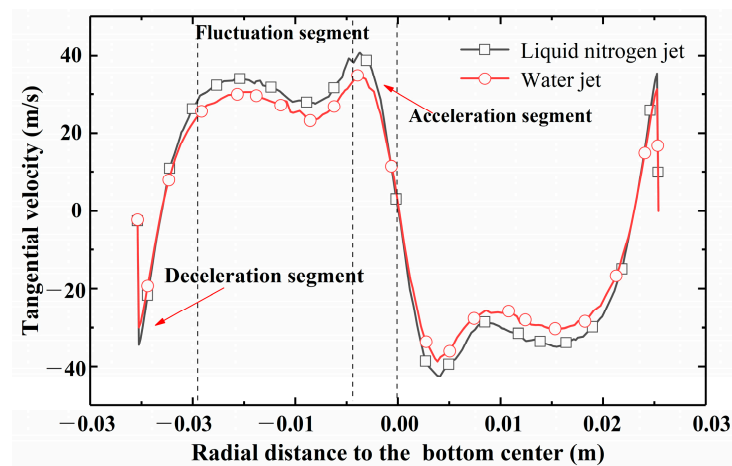


Figure 5. Curve of tangential velocity in the bottomhole.

3.4. Thermal Stress

Given that the water jet's temperature is significantly higher than that of the liquid nitrogen jet and its temperature gradient is smaller, its thermal stress effects on the rock are less pronounced than those caused by the liquid nitrogen jet. This study analyzes the liquid nitrogen jet to more clearly observe its unique effects. Figure 6 shows that this study examines rock layers at depths of 2 and 10 mm. Under thermal stress, the variation in the maximum principal stress over time at these two depths exhibits a trend similar to that observed under thermomechanical coupling. The maximum principal stress within the rock at a 2 mm depth rapidly increases from 2 to 10 s, then decelerates after 10 s, and slightly decreases at 120 s. In contrast, the maximum principal stress within the rock at 10 mm depth demonstrates a continuous upward trend, although slower. This shows that thermal stress significantly affects the rock layer at 2 mm depth. Comparatively, previous findings indicate that under the impact of the liquid nitrogen jet, the maximum principal stress of the rock at 2 mm depth is nearly negative at 1 s under thermomechanical coupling. This indicates that the rock is initially in compression, which transitions to tension after 10 s, aligning with the thermal stress trend. In the rock layer at 2 mm depth, the maximum principal stress at the jet center changes by about 9.627 MPa from 1 to 10 s under thermomechanical coupling, with approximately 8.168 MPa of this change attributed to thermal stress, accounting for 84.8% of the total change magnitude. This underscores that thermal stress plays a significant supportive role in the tensile failure of the rock. Figure 7 further illustrates the changes in Mises stress of rocks at different depths under thermal stress. Specifically, for the rock sample at 2 mm depth, the Mises stress at the center reaches a minimum at 1 s, then gradually increases in the radial direction. At 10 s, the trend rapidly changes so that the stress at the center reaches its maximum value, then gradually decreases along the radial direction. During this period, the Mises stress at the center increases by 5.516 MPa, while under thermomechanical coupling, this increase reaches 9.62 MPa, marking an increase of about 40%. This indicates a significant contribution of thermal stress to Mises stress, reinforcing its pivotal role in the shear failure of the rock.

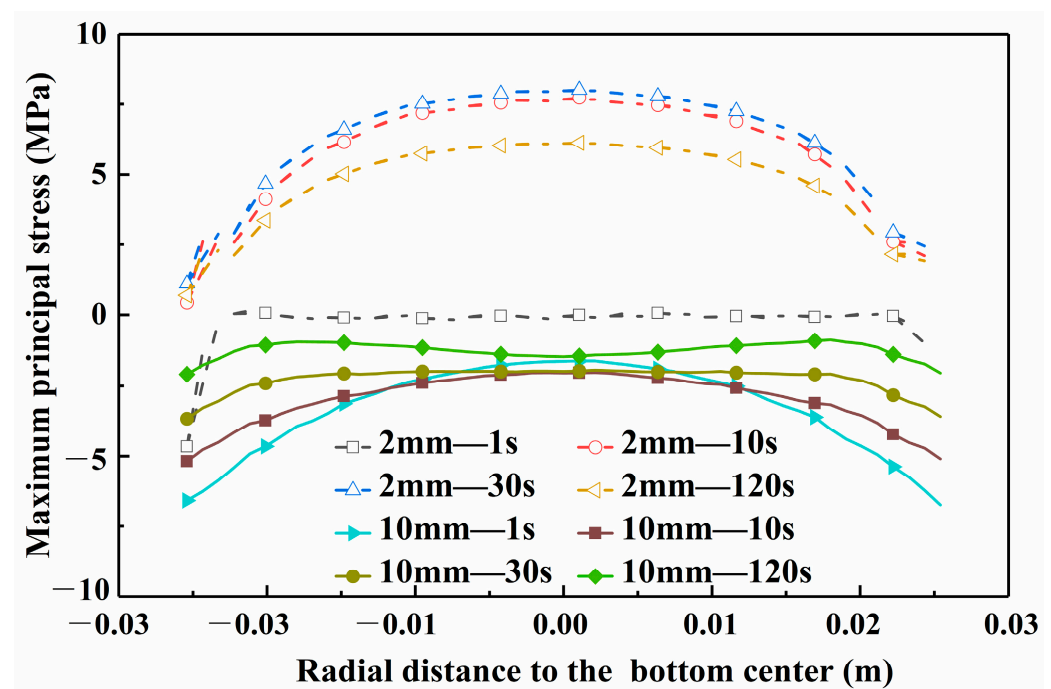


Figure 6. Maximum principal stress distribution of liquid nitrogen jet in radial direction in the bottomhole under the effect of temperature.

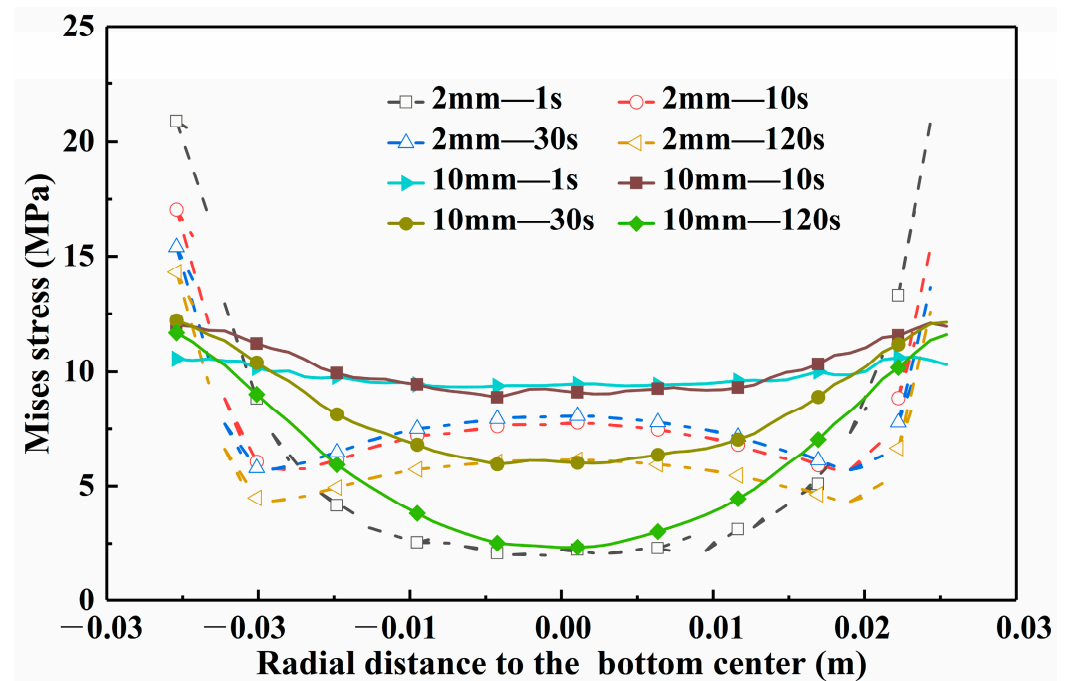


Figure 7. Mises stress distribution of liquid nitrogen jet in radial direction in the bottomhole under the effect of temperature.

4. Analysis of the Influence of Parameters on Stress Distribution in the Rock in the Bottomhole Under the Impact of a Liquid Nitrogen Jet

4.1. Parameter Selection

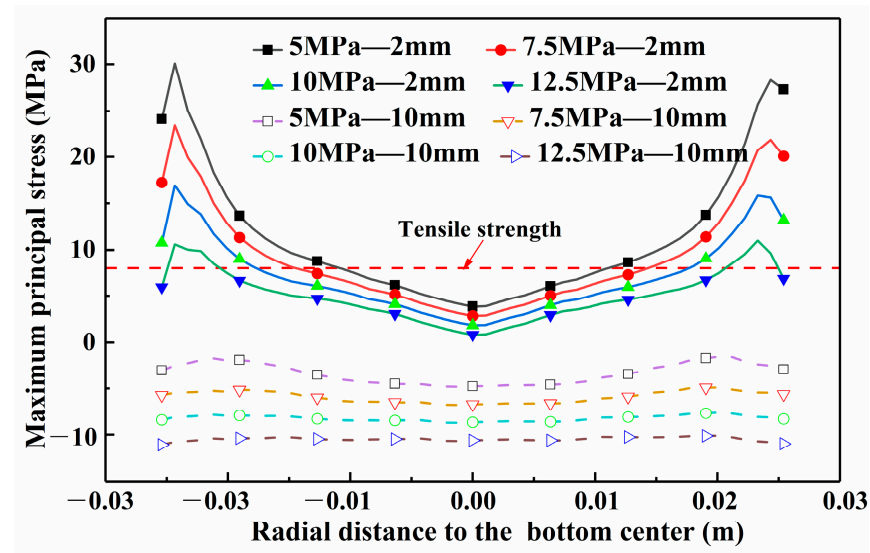
Previous research indicates that the stress field in rock is influenced by impact pressure and thermal stress under the effect of the liquid nitrogen jet. According to the governing equations, four rock parameters, confining pressure, elastic modulus, Poisson's ratio, and rock temperature, affect the internal stress field within the rock. The impact pressure of the jet is directly influenced by jet velocity, which is related to the inlet and outlet pressures of the jet. Therefore, it is necessary to investigate the influence of rock confining pressure, elastic modulus, Poisson's ratio, and rock temperature, as well as the inlet pressure and temperature of the fluid, on rock stress. The studied parameter ranges may not fully cover all possible conditions encountered in real-world applications. For example, rock properties and fluid conditions can vary widely in different geological formations and drilling operations. However, the conclusions drawn from this range could provide valuable insights into the stress distribution characteristics of rock under liquid nitrogen jet impact.

4.2. Influence of Solid Parameters on Stress Distribution

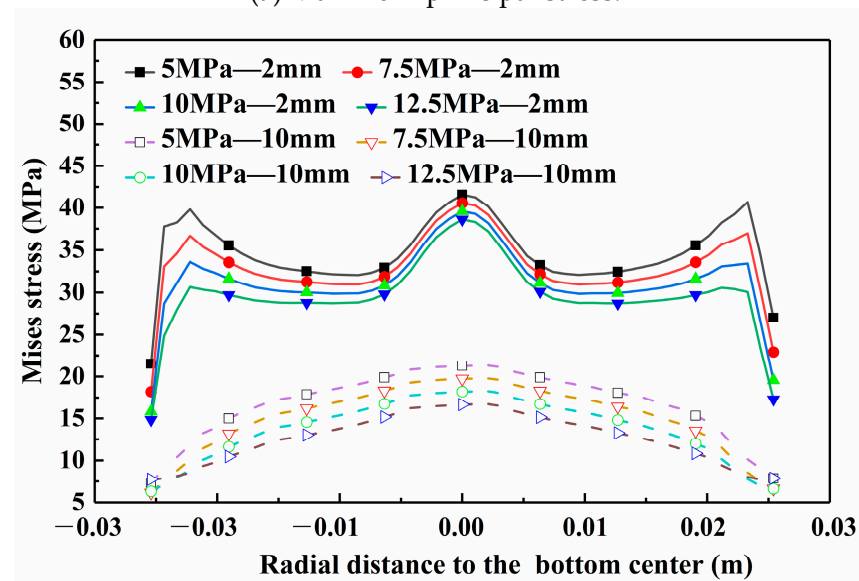
4.2.1. Influence of Rock Confining Pressure on Stress Distribution

The stress distributions of the rock at the bottomhole under different confining pressure conditions are obtained by adjusting and recalculating the rock confining pressure in the basic numerical example, as illustrated in Figure 8. As the confining pressure increases, both the maximum principal stress and Mises stress in the rock exhibit a trend of gradual decrease, with the magnitude of change at the center point of the bottomhole being relatively small. Specifically, when the rock confining pressure increases from 5 MPa to 12.5 MPa, the peak maximum principal stress at 2 mm depth decreases from 30.09 MPa to 9.86 MPa. This indicates that an increase of 7.5 MPa in confining pressure reduces 20.23 MPa in maximum principal stress, with a change magnitude ratio of approximately 270% between the confining pressure and the maximum principal stress. This indicates that rock confining pressure significantly affects the maximum principal stress at 2 mm depth. At 10 mm depth, the peak maximum principal stress decreases from -1.71 to -10.42 MPa, with a change magnitude ratio of approximately 139%. A positive value of maximum principal stress

indicates a tensile state, while a negative value indicates a compressive state. The reduction in maximum principal stress indicates a gradual decrease in tensile stress, showing a clear trend of transitioning toward compressive stress. Since rock has greater compression resistance than tension, tensile failure predominates, aligning with the damage region assessment methods discussed in Chapter 4. The red dashed line in Figure 8a indicates the tensile failure limit of granite, which is 8 MPa. As confining pressure increases, the range of maximum principal stress exceeding the tensile failure limit decreases gradually, from 19.417 mm at 5 MPa to 8.897 mm at 12.5 MPa, a reduction of 121.6%. This shows that a higher confining pressure inhibits tensile failure, while a lower confining pressure promotes tensile failure under the impact of the liquid nitrogen jet. The changes in Mises stress show that the peak stress of the rocks at 2 mm and 10 mm depths does not vary significantly with the confining pressure. At 10 mm depth, the change in the peak Mises stress is only 4.6 MPa, indicating that confining pressure has a smaller effect on Mises stress than on maximum principal stress. This further demonstrates that variations in confining pressure have a limited impact on the shear failure of rock under the influence of the liquid nitrogen jet.



(a) Maximum principal stress.



(b) Mises stress

Figure 8. Influence of rock confining pressure on stress distribution.

4.2.2. Influence of Elastic Modulus and Poisson's Ratio of the Rock on Stress Distribution

The stress distributions of the rock at the bottomhole under different parameter conditions are obtained by adjusting the elastic modulus and Poisson's ratio of the rock in the basic numerical example, as illustrated in Figures 9 and 10. The elastic modulus has a more pronounced effect on the changes in the rock stress field, which is reflected in larger stress variations, whereas the influence of Poisson's ratio is smaller. This difference is particularly significant at 2 mm depth.

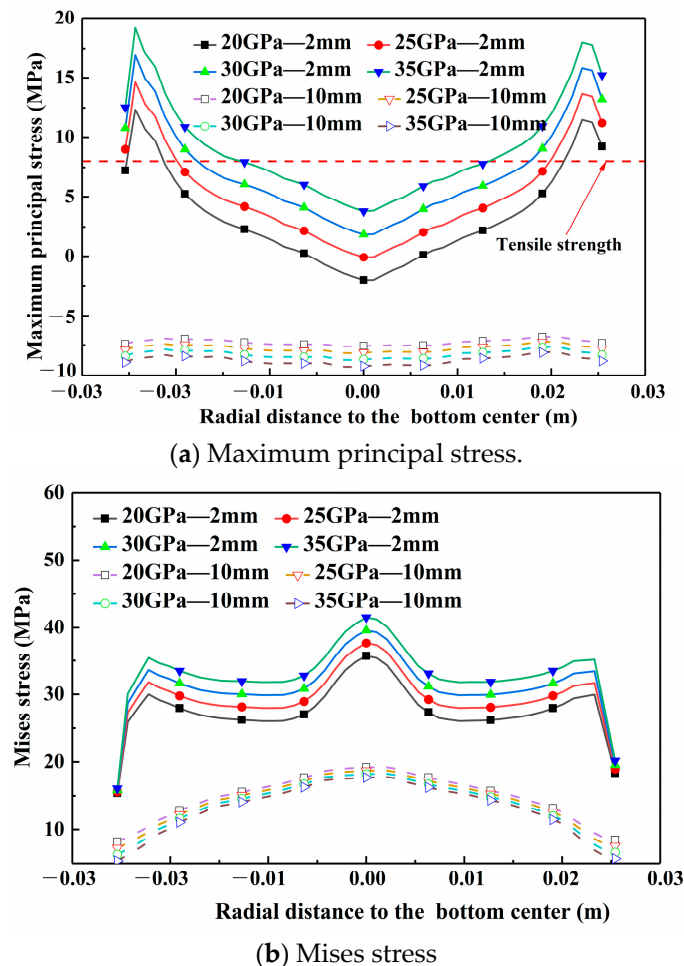


Figure 9. Influence of elastic modulus on stress distribution.

Figure 9a demonstrates that with the impact center point in the bottomhole used as the study object, the maximum principal stress at a depth of 2 mm increases significantly from -2.026 MPa to 3.787 GPa when the elastic modulus rises from 20 to 35 GPa, representing a 289% increase. The red dashed line in the figure indicates a tensile failure limit of 8 MPa for the rock. As the elastic modulus increases, the tensile failure zone expands from 8.793 to 16.242 mm, showing an 84% increase. With each 5 GPa increase in the elastic modulus, the maximum principal stress increases further. Similarly, the stress at the center point at a depth of 10 mm gradually rises with the elastic modulus, representing a 22% increase. This indicates that rocks with higher elastic modulus values are more prone to tensile failure under the impact of a liquid nitrogen jet, leading to increased tensile stress.

Figure 9b reveals that the Mises stress at the impact center point increases by 16.3% at a 2 mm depth and decreases by 8.5% at a 10 mm depth. This further demonstrates that a larger elastic modulus enhances the shear failure of shallow rocks under the impact of a liquid nitrogen jet while suppressing shear failure in deeper rocks.

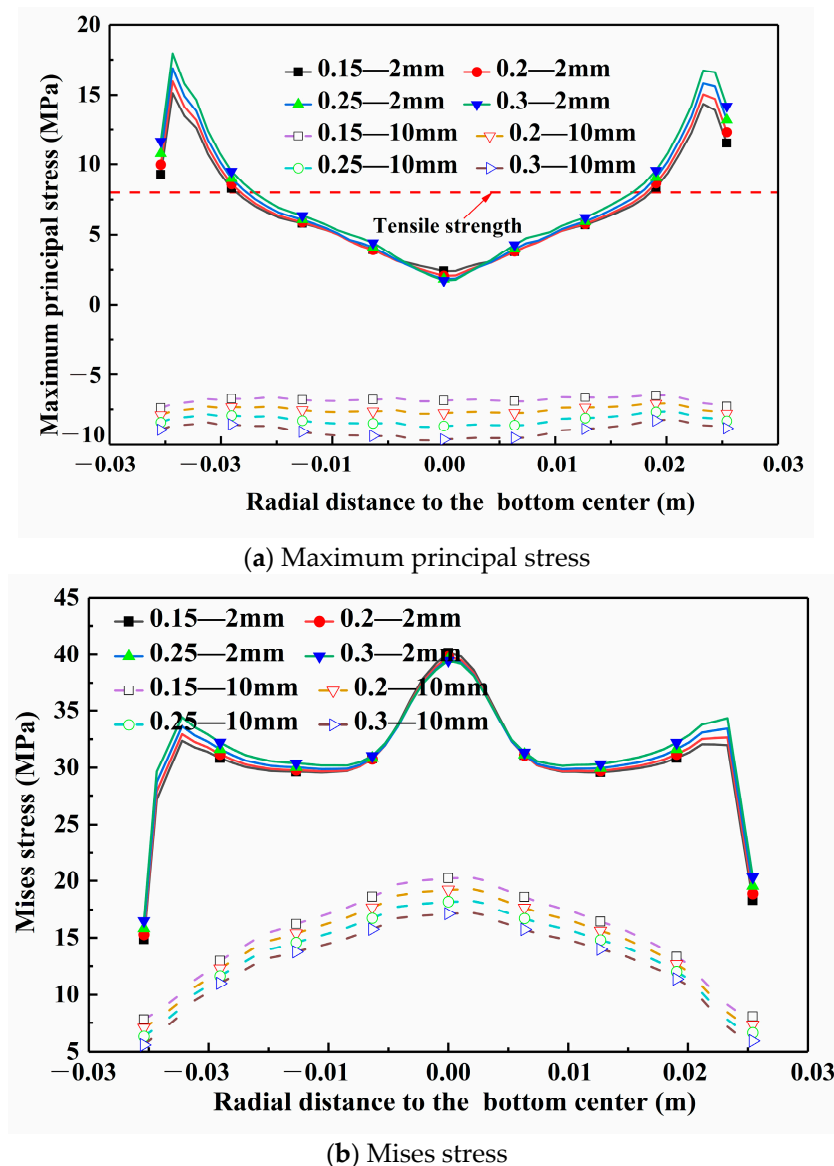


Figure 10. Influence of Poisson's ratio on stress distribution.

Figure 10 shows that the maximum principal stress and Mises stress at the center point at a depth of 2 mm only increase slightly, while the tensile failure zone expands from 10.92 mm at a Poisson's ratio of 0.15 to 13.067 mm at a Poisson's ratio of 0.3. The change in rock stress at the center point at the 10 mm depth is more pronounced than that at the 2 mm depth, with the maximum principal stress increasing from -7.76 to -9.64 MPa, indicating increased compressive stress. This shows that at a larger Poisson's ratio, the liquid nitrogen jet has minimal impact on the maximum principal stress of shallow rocks, with only a slight effect on the expansion of the damage zone. In addition, deeper rocks with higher Poisson's ratios experience greater compressive stress under the impact of the liquid nitrogen jet, which is unfavorable for rock failure.

4.2.3. Influence of Initial Rock Temperature on Stress Distribution

Figure 11 indicates that the trends in Mises stress and maximum principal stress with increasing temperature vary by depth. At a depth of 2 mm, the maximum principal stress at the impact center point increases from -0.144 MPa at 50 °C to 1.849 MPa at 150 °C, then decreases to 0.621 MPa as the temperature continues to rise to 200 °C, with the tensile failure zone reaching its largest extent at 150 °C. In contrast, at a depth of 10 mm, the

maximum principal stress at the impact center point increases from -5.399 MPa at 50°C to -10.768 MPa at 200°C , showing a 99.46% increase. The change in Mises stress at a 2 mm depth exhibits a similar trend of initial increase followed by a decrease, while at 10 mm depth, it gradually decreases with rising temperature.

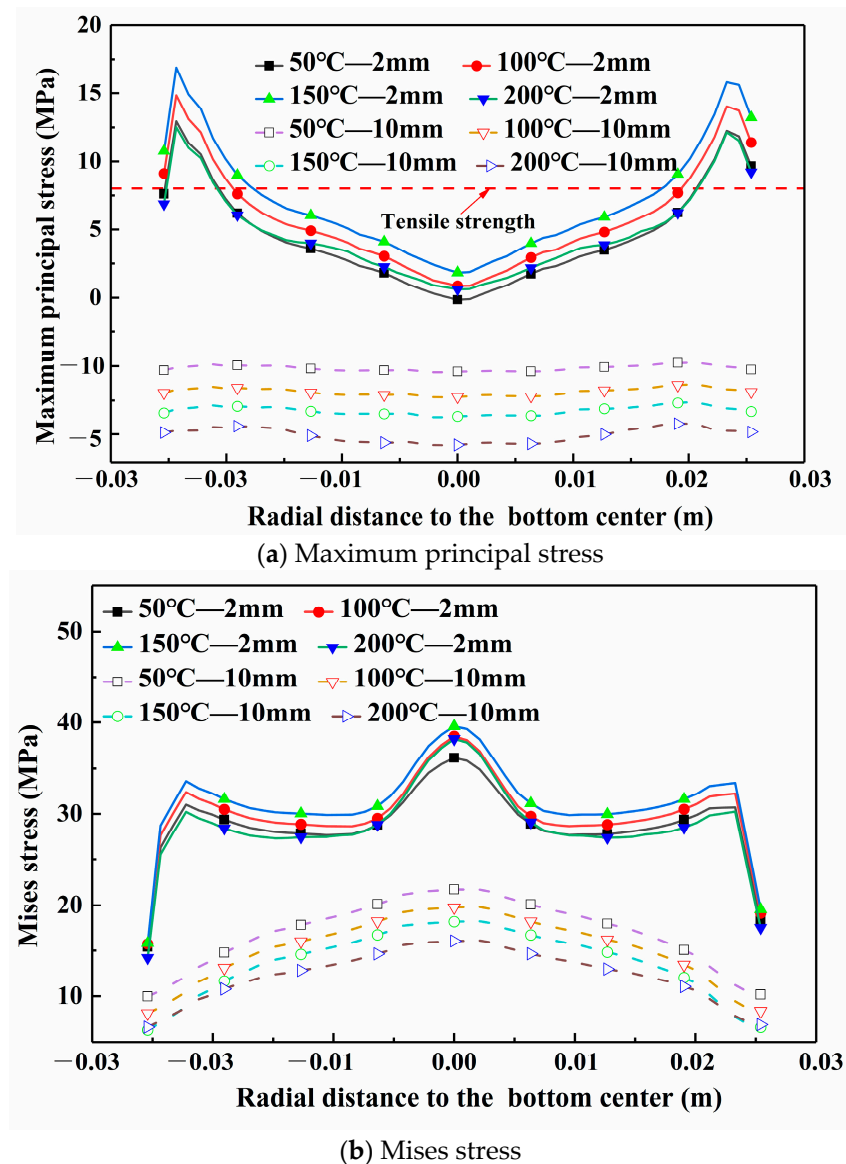


Figure 11. Influence of initial rock temperature on stress distribution.

4.3. Influence of Fluid Parameters on Stress Distribution

4.3.1. Influence of Outlet Pressure on Stress Distribution

Figure 12 demonstrates that unlike the trends observed with solid parameters, the changes in maximum principal stress under varying outlet pressures are insignificant. At outlet pressures of 35 and 40 MPa, the maximum principal stress of the rock at a depth of 2 mm decreases as the pressure increases, while the changes at a depth of 10 mm are minimal. The maximum principal stress range at the impact center point is 2.855 MPa at a 2 mm depth and 1.286 MPa at a 10 mm depth. The tensile failure zone does not reach its limit before 40 MPa but at 45 MPa, with the damage zone increasing from 6.008 to 7.067 mm as the pressure rises. This indicates that variation in outlet pressure between 40 and 45 MPa significantly affects the expansion of the tensile failure zone.

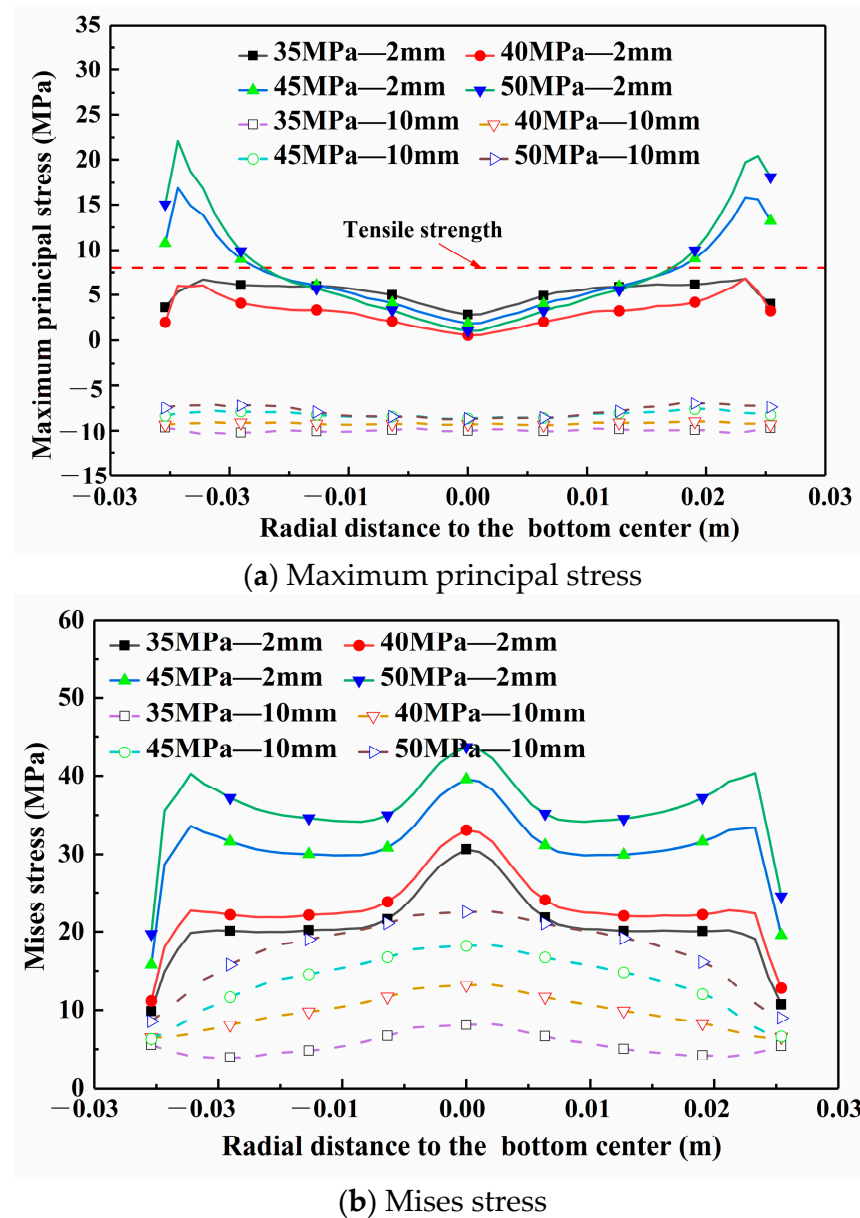


Figure 12. Influence of outlet pressure on stress distribution.

The changes in Mises stress are significant. For instance, at the impact center point of the jets, it increases from 21.805 to 43.711 MPa at a 2 mm depth, with an increase of 19.906 MPa, while at a 10 mm depth, it increases from 8.1024 to 22.513 MPa, representing an increase of 14.411 MPa. When the outlet pressure increases by 5 MPa, the most significant change in Mises stress occurs between 40 and 45 MPa, indicating that this pressure range has the greatest effect on the Mises stress and shear failure of the rock. This is consistent with the outlet pressure range that most influences the expansion of the tensile failure zone.

4.3.2. Influence of Fluid Temperature on Stress Distribution

Figure 13 shows that the maximum principal stress distribution does not change significantly with increasing temperature. It maintains a pattern of compression at the center and tension at both ends, generated by stress concentrations at the impact center and the two ends of the bottomhole. Similarly, Mises stress also does not change significantly with increasing temperature. Stress concentration occurs near the bottomhole plane, with a trend of decreasing radially and then increasing at both ends.

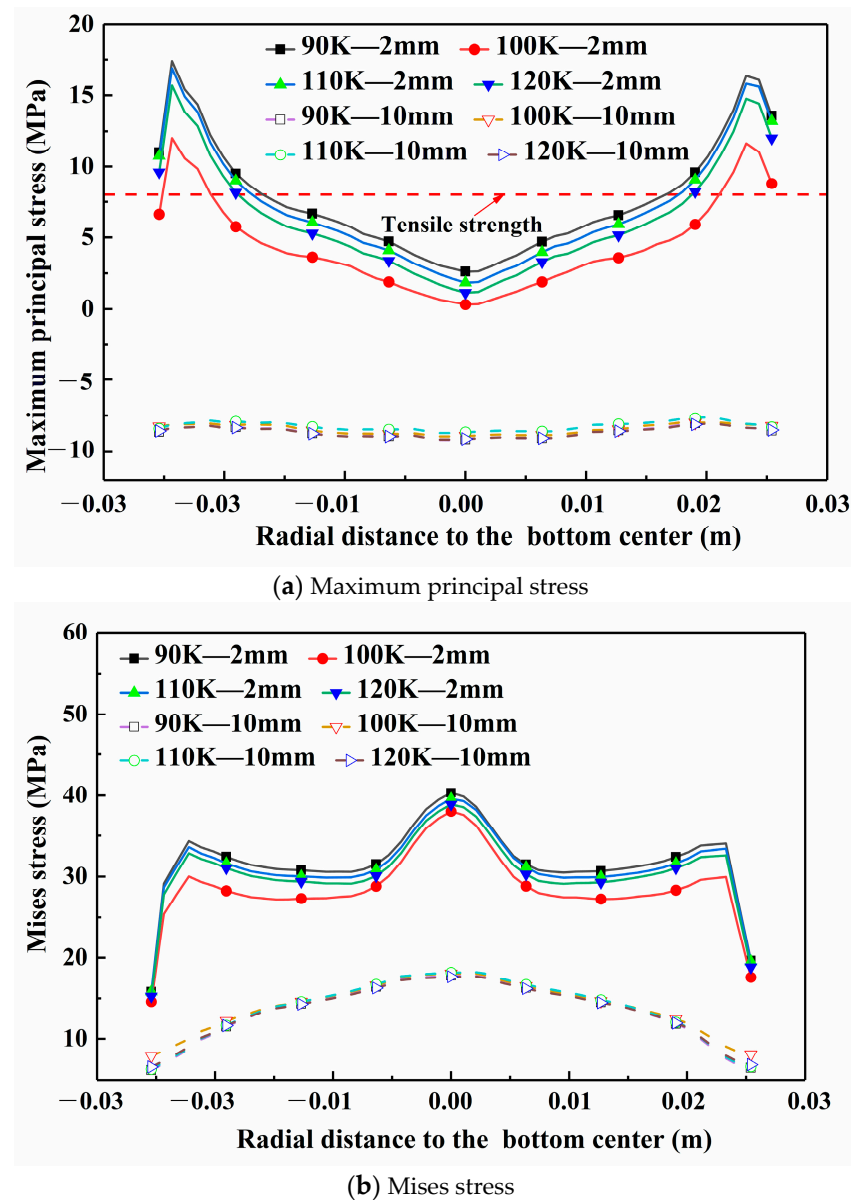


Figure 13. Influence of fluid temperature on stress distribution.

The maximum principal and Mises stresses remain essentially unchanged at a depth of 10 mm. However, at a depth of 2 mm, they reach their maximum at 90 K, decrease at 100 K, increase at 110 K, and decrease again at 120 K, indicating an unstable trend with significant fluctuations. The tensile failure zone exhibits a similar trend to the stress changes, with damage zones measuring 7.067, 2.833, 6.01, and 4.96 mm as fluid temperature increases. The volatility in the influence of fluid temperature on stress distribution can be due to a small temperature change gradient. In this case, the temperature change between adjacent test groups is 10 K, while in the previous study on the influence of rock temperature, the temperature change between adjacent groups was 50 °C, leading to a more distinct pattern of change.

5. Advantages of Drilling with Liquid Nitrogen

Based on the findings of this study on the stress distribution characteristics of rock in the bottomhole and the influence laws of various parameters under the impact of a liquid nitrogen jet, the potential economic benefits and environmental impacts of implementing optimized liquid nitrogen jet drilling techniques can be analyzed as follows:

5.1. Potential Economic Benefits

This study indicates that liquid nitrogen jet drilling can enhance rock-breaking efficiency due to the thermal stress created by its extremely low temperature. This could lead to faster drilling rates, reducing the time and cost associated with drilling operations. Compared to traditional hydraulic drilling, liquid nitrogen jet drilling does not require large volumes of water, which could reduce energy consumption associated with water transportation and treatment. The ability of liquid nitrogen to effectively create and propagate fractures within the reservoir rock can lead to improved reservoir permeability and production capacity, potentially extending the life of the reservoir and increasing its economic value.

5.2. Comparison to Existing Technologies

The economic benefits can be quantified through a cost–benefit analysis that compares the initial investment, operational costs, and potential revenue gains from increased production between liquid nitrogen jet drilling and existing technologies such as hydraulic drilling. The environmental impact, particularly related to energy use and greenhouse gas emissions, can be assessed by comparing the life cycle energy consumption and carbon footprint of liquid nitrogen jet drilling with those of traditional methods. This would involve considering the energy required for producing, transporting, and utilizing liquid nitrogen, as well as the impacts of reduced water use.

5.3. Environmental Impacts

One of the key environmental benefits is the reduced reliance on water, which is particularly important in water-scarce regions. This can alleviate the pressure on local water resources and reduce the potential for water contamination associated with hydraulic fracturing. The use of liquid nitrogen may result in lower greenhouse gas emissions compared to hydraulic drilling, primarily due to the elimination of large-scale water usage and associated energy consumption. However, a complete life cycle assessment would need to consider the emissions associated with liquid nitrogen production and transportation.

6. Conclusions

- (1) Due to lower kinetic viscosity, the liquid nitrogen jet experiences less energy dissipation and achieves a significantly higher maximum velocity than the water jet under the same conditions, with an axial velocity about 20 m/s higher.
- (2) Both water and liquid nitrogen jets have high-pressure regions concentrated at the bottomhole center, with comparable pressure magnitudes and impact forces. The pressure at the center is twice that at the ends, causing significant rock compression.
- (3) Both jets exhibit similar tangential velocity distributions with high-velocity overflow at the bottomhole center, but the liquid nitrogen jet's maximum velocity is 20% higher. This overflow boosts heat exchange efficiency, which is crucial for thermal rock fracturing.
- (4) The rate of stress change in rock under the liquid nitrogen jet is significantly higher than that under the water jet, especially within the first 10 s. At 2 mm depth, the liquid nitrogen jet induces tensile stress, making it more effective at causing tensile failure and promoting rock fracturing.
- (5) The Mises stress from the water jet is concentrated at the impact center, while the liquid nitrogen jet shows a broader stress distribution, leading to a larger rock fracturing region.

Author Contributions: Methodology, C.C. and B.X.; conceptualization, C.C.; investigation, B.W. and Y.F.; data curation, Z.Z. and J.L.; writing—original draft, C.C. and B.X.; writing—review and editing, B.W. and Y.G.; funding acquisition, Y.G. All authors have read and agreed to the published version of the manuscript.

Funding: This research was supported by the Yunlong Lake Laboratory of Deep Underground Science and Engineering Project (No. 104024001) and Sinopec Key Laboratory of Shale Oil and Gas Drilling and Hydraulic Fracturing (No. 36650000-23-ZC0609-0025).

Data Availability Statement: Data will be made available on request.

Conflicts of Interest: Author Bo Xiao was employed by the company Sinopec Research Institute of Petroleum Engineering Co., Ltd. The remaining authors declare that the research was conducted in the absence of any commercial or financial relationships that could be construed as a potential conflict of interest.

References

- Li, Y.; Wang, H.; Wang, Y.; Zhao, J. Background and routs of carbon neutrality and its nature-derived thermal solutions. *Huadian Technol.* **2021**, *43*, 5–14.
- Wang, G.; Zhang, W.; Liang, J.; Lin, W.; Liu, Z.; Wang, W. Evaluation of Geothermal Resources Potential in China. *Acta Geosci. Sin.* **2017**, *38*, 449–450.
- Lei, H. Coupling Mechanics with Thermal-Hydrodynamic Processes for Heat Development in Enhanced Geothermal Systems (EGS). Doctoral Thesis, Jilin University, Changchun, China, 2014.
- Rauenzahn, R.M.; Tester, J.W. Rock failure mechanisms of flame-jet thermal spallation drilling-theory and experimental testing. *Int. J. Rock Mech. Min. Sci. Geomech. Abstr.* **1989**, *26*, 381–399. [[CrossRef](#)]
- Hu, X.; Song, X.; Li, G.; Shen, Z.; Lyu, Z.; Shi, Y. Shape factor of the flake-like particle in thermal spallation and its effects on settling and transport behavior in drilling annulus. *Powder Technol.* **2018**, *335*, 211–221. [[CrossRef](#)]
- Wang, H.; Li, G.; Shen, Z. A Feasibility Analysis on Shale Gas Exploitation with Supercritical Carbon Dioxide. *Energy Sources Part A Recover. Util. Environ. Eff.* **2012**, *34*, 1426–1435. [[CrossRef](#)]
- Wang, H.; Li, G.; Shen, Z.; Tian, S.; Sun, B.; He, Z.; Lu, P. Experiment on rock breaking with supercritical carbon dioxide jet. *J. Pet. Sci. Eng.* **2015**, *127*, 305–310. [[CrossRef](#)]
- Zhao, X.; Huang, B.; Xu, J. Experimental investigation on the characteristics of fractures initiation and propagation for gas fracturing by using air as fracturing fluid under true triaxial stresses. *Fuel* **2018**, *236*, 1496–1504. [[CrossRef](#)]
- Wang, L.; Yao, B.; Cha, M.; Alqahtani, N.B.; Patterson, T.W.; Kneafsey, T.J.; Miskimins, J.L.; Yin, X.; Wu, Y.-S. Waterless fracturing technologies for unconventional reservoirs-opportunities for liquid nitrogen. *J. Nat. Gas Sci. Eng.* **2016**, *35*, 160–174. [[CrossRef](#)]
- Kim, K.M.; Kemeny, J. Effect of thermal shock and rapid unloading on mechanical rock properties. In Proceedings of the 43rd US Rock Mechanics Symposium & 4th US-Canada Rock Mechanics Symposium, Asheville, NC, USA, 28 June–1 July 2009; American Rock Mechanics Association: Seattle, WA, USA, 2009.
- Brown, D.W.; Duchane, D.V. Scientific progress on the Fenton Hill HDR project since 1983. *Geothermics* **1999**, *28*, 591–601. [[CrossRef](#)]
- McDaniel, B.W.; Grundmann, S.R.; Kendrick, W.D.; Wilson, D.R.; Jordan, S.W. Field applications of cryogenic nitrogen as a hydraulic fracturing fluid. In Proceedings of the SPE Annual Technical Conference and Exhibition, San Antonio, TX, USA, 5–8 October 1997; Society of Petroleum Engineers: Richardson, TX, USA, 1997.
- Grundmann, S.R.; Rodvelt, G.D.; Dials, G.A. Cryogenic nitrogen as a hydraulic fracturing fluid in the Devonian Shale. In Proceedings of the SPE Eastern Regional Meeting, Pittsburgh, PA, USA, 9–11 November 1998; Society of Petroleum Engineers: Richardson, TX, USA, 1998.
- Finnie, I.; Cooper, G.A.; Berlie, J. Fracture propagation in rock by transient cooling. *Int. J. Rock Mech. Min. Sci. Geomech. Abstr.* **1979**, *16*, 11–21. [[CrossRef](#)]
- Ren, S.; Fan, Z.; Zhang, L. Mechanisms and Experimental Study of Thermal-shock Effect on Coal-rock Using Liquid Nitrogen. *Chin. J. Rock Mech. Eng.* **2013**, *32*, 3790–3794.
- Kim, K.; Kemeny, J.; Nickerson, M. Effect of Rapid Thermal Cooling on Mechanical Rock Properties. *Rock Mech. Rock Eng.* **2014**, *47*, 2005–2019. [[CrossRef](#)]
- Cai, C.; Li, G.; Huang, Z.; Tian, S.; Shen, Z.; Fu, X. Experiment of coal damage due to super-cooling with liquid nitrogen. *J. Nat. Gas Sci. Eng.* **2015**, *22*, 42–48. [[CrossRef](#)]
- Cha, M.; Yin, X.; Kneafsey, T.; Johanson, B.; Alqahtani, N.; Miskimins, J.; Patterson, T.; Wu, Y.-S. Cryogenic fracturing for reservoir stimulation—Laboratory studies. *J. Pet. Sci. Eng.* **2014**, *124*, 436–450. [[CrossRef](#)]
- Cai, C.; Huang, Z.; Li, G.; Gao, F. Particle velocity distributions of abrasive liquid nitrogen jet and parametric sensitivity analysis. *J. Nat. Gas Sci. Eng.* **2015**, *27*, 1657–1666. [[CrossRef](#)]
- Cai, C.; Huang, Z.; Li, G.; Gao, F.; Wei, J.; Li, R. Feasibility of reservoir fracturing stimulation with liquid nitrogen jet. *J. Pet. Sci. Eng.* **2016**, *144*, 59–65. [[CrossRef](#)]
- Zhang, C.; Wang, L.; Zhao, Q.; Li, W. Permeability evolution model and numerical analysis of coupled coal deformation, failure and liquid nitrogen cooling. *J. Hebei Univ. Sci. Technol.* **2015**, *36*, 90–99.
- Huang, Z.; Cai, C.; Li, G.; Tian, S. Flow behavior and particle acceleration effect of abrasive liquid nitrogen jet. *J. China Univ. Pet. (Ed. Nat. Sci.)* **2016**, *40*, 80–86.
- Li, Z.; Xu, H.; Zhang, C. Liquid nitrogen gasification fracturing technology for shale gas development. *J. Pet. Sci. Eng.* **2016**, *138*, 253–256. [[CrossRef](#)]
- Zhai, C.; Qin, L.; Liu, S.; Xu, J.; Tang, Z.; Wu, S. Pore Structure in Coal: Pore Evolution after Cryogenic Freezing with Cyclic Liquid Nitrogen Injection and Its Implication on Coalbed Methane Extraction. *Energy Fuels* **2016**, *30*, 6009–6020. [[CrossRef](#)]

25. Zhai, C.; Wu, S.; Liu, S.; Qin, L.; Xu, J. Experimental study on coal pore structure deterioration under freeze–thaw cycles. *Environ. Earth Sci.* **2017**, *76*, 1–12. [\[CrossRef\]](#)
26. Yao, B.; Wang, L.; Yin, X.; Wu, Y.-S. Numerical modeling of cryogenic fracturing process on laboratory-scale Niobrara shale samples. *J. Nat. Gas Sci. Eng.* **2017**, *48*, 169–177. [\[CrossRef\]](#)
27. Cai, C.; Gao, F.; Huang, Z.; Yang, Y. Numerical simulation on the flow field characteristics and impact capability of liquid nitrogen jet. *Energy Explor. Exploit.* **2018**, *36*, 989–1005. [\[CrossRef\]](#)
28. Cai, C.; Yang, Y.; Liu, J.; Gao, F.; Gao, Y.; Zhang, Z. Downhole Transient Flow Field and Heat Transfer Characteristics During Drilling with Liquid Nitrogen Jet. *J. Energy Resour. Technol.* **2018**, *140*, 12290212. [\[CrossRef\]](#)
29. Wu, X.; Huang, Z.; Li, G.; Li, R.; Yan, P.; Deng, X.; Mu, K.; Dai, X. Experiment on coal breaking with cryogenic nitrogen jet. *J. Pet. Sci. Eng.* **2018**, *169*, 405–415. [\[CrossRef\]](#)
30. Zhang, S.; Huang, Z.; Li, G.; Wu, X.; Peng, C.; Zhang, W. Numerical analysis of transient conjugate heat transfer and thermal stress distribution in geothermal drilling with high-pressure liquid nitrogen jet. *Appl. Therm. Eng.* **2018**, *129*, 1348–1357. [\[CrossRef\]](#)
31. Zhang, S.; Huang, Z.; Wang, H.; Zhang, H.; Zhang, C.; Xiong, C. Thermal characteristics analysis with local thermal non-equilibrium model during liquid nitrogen jet fracturing for HDR reservoirs. *Appl. Therm. Eng.* **2018**, *143*, 482–492. [\[CrossRef\]](#)
32. Zhang, S.; Huang, Z.; Huang, P.; Wu, X.; Xiong, C.; Zhang, C. Numerical and experimental analysis of hot dry rock fracturing stimulation with high-pressure abrasive liquid nitrogen jet. *J. Pet. Sci. Eng.* **2018**, *163*, 156–165. [\[CrossRef\]](#)
33. Zhang, S.; Huang, Z.; Wang, H.; Li, G.; Sepehrnoori, K.; Wu, X.; Hong, C. Experimental study on the rock-breaking characteristics of abrasive liquid nitrogen jet for hot dry rock. *J. Pet. Sci. Eng.* **2019**, *181*, 106166. [\[CrossRef\]](#)
34. Yang, R.; Hong, C.; Huang, Z.; Song, X.; Zhang, S.; Wen, H. Coal breakage using abrasive liquid nitrogen jet and its implications for coalbed methane recovery. *Appl. Energy* **2019**, *253*, 113485. [\[CrossRef\]](#)
35. Liu, J.; Li, J.; Long, W.; Yuting, C.; Jin, Y. Failure analysis of water liquid nitrogen cyclic jet impacting concrete. *Int. J. Mech. Sci.* **2022**, *235*, 107714. [\[CrossRef\]](#)
36. Wang, Y.; Dai, M.; Liu, K.; Liu, J.; Han, L.; Liu, H. Research on surface heat transfer mechanism of liquid nitrogen jet cooling in cryogenic machining. *Appl. Therm. Eng.* **2020**, *179*, 115607. [\[CrossRef\]](#)
37. Dai, X.; Huang, Z.; Wu, X.; Shi, H.; Xiong, C. Failure Analysis of High-Temperature Granite Under the Joint Action of Cutting and Liquid Nitrogen Jet Impingement. *Rock Mech. Rock Eng.* **2021**, *54*, 6249–6264. [\[CrossRef\]](#)
38. Cai, C.; Wang, B.; Huang, Z.; Yue, W.; Wang, H.; Gao, Y.; Feng, Y.; Yang, Y.; Guo, C. Comparison with the effect of the cyclic liquid nitrogen jet and liquid nitrogen immersion cooling on the deterioration of mechanical properties of high temperature rocks. *Geoenergy Sci. Eng.* **2024**, *243*, 213295. [\[CrossRef\]](#)
39. Li, R.; Yan, Y.; Huang, Z. Thermal and mechanical analysis of LN2 jet impinging on rock surface. *Appl. Therm. Eng.* **2020**, *178*, 115581. [\[CrossRef\]](#)

Disclaimer/Publisher’s Note: The statements, opinions and data contained in all publications are solely those of the individual author(s) and contributor(s) and not of MDPI and/or the editor(s). MDPI and/or the editor(s) disclaim responsibility for any injury to people or property resulting from any ideas, methods, instructions or products referred to in the content.